How to cite: *Angew. Chem. Int. Ed.* **2024**, *63*, e202400382
doi.org/10.1002/anie.202400382

Energy Storage

One-Pot Synthesis of High-Capacity Sulfur Cathodes via In-Situ Polymerization of a Porous Imine-Based Polymer

Guiping Li, Ye Liu, Thorsten Schultz, Moritz Exner, Ruslan Muydinov, Hui Wang, Kerstin Scheurell, Jieyang Huang, Paulina Szymoniak, Nicola Pinna, Norbert Koch, Philipp Adelhelm, and Michael J. Bojdys**

Abstract: Lithium-ion batteries, essential for electronics and electric vehicles, predominantly use cathodes made from critical materials like cobalt. Sulfur-based cathodes, offering a high theoretical capacity of 1675 $mAh\,g^{-1}$ and environmental advantages due to sulfur's abundance and lower toxicity, present a more sustainable alternative. However, state-of-the-art sulfur-based electrodes do not reach the theoretical capacities, mainly because conventional electrode production relies on mixing of components into weakly coordinated slurries. Consequently, sulfur's mobility leads to battery degradation—an effect known as the "sulfur-shuttle". This study introduces a solution by developing a microporous, covalently-bonded, imine-based polymer network grown in situ around sulfur particles on the current collector. The polymer network (i) enables selective transport of electrolyte and Li-ions through pores of defined size, and (ii) acts as a robust host to retain the active component of the electrode (sulfur species). The resulting cathode has superior rate performance from 0.1 C (1360 $mAh\,g^{-1}$) to 3 C (807 $mAh\,g^{-1}$). Demonstrating a high-performance, sustainable sulfur cathode produced via a simple one-pot process, our research underlines the potential of microporous polymers in addressing sulfur diffusion issues, paving the way for sulfur electrodes as viable alternatives to traditional metal-based cathodes.

Introduction

Cost-effective, high-performance and secure lithium-ion batteries (LIBs) are required to meet the growing demand for portable electronic devices and the transition to electric mobility.[1] Among the commercial LIBs in the market, there are several types of lithium multi-metal oxide materials,[2] and it is clear that today's metal oxides have inherent capacity limits. In addition, the rapidly growing prices for key metals, such as cobalt and lithium, necessitate that we explore alternative materials for the next generation of batteries.[3] The lithium-sulfur (Li–S) battery has received tremendous attention—because in theory and according to calculations—they have exceedingly high specific capacities of 1675 $mAh\,g^{-1}$ (or 2550 $Wh\,kg^{-1}$).[4] Furthermore, sulfur is widely available as byproduct from petroleum refinement,[5] it is low cost and environmental friendly. However, Li–S battery encounters arduous challenges for practical applications which still suffers from several detrimental issues, such as "shuttle effect" of lithium polysulfides, intrinsic low electrical conductivity of sulfur (5×10^{-30} $S\,cm^{-1}$ at 25 °C) and lithium sulfide (Li_2S, 3×10^{-7} $S\,cm^{-1}$), a large volumetric fluctuation (~80 %) during lithiation, attributed to the conversion from S (2.03 $g\,cm^{-3}$) to Li_2S (1.63 $g\,cm^{-3}$), which

[*] G. Li, Prof. M. J. Bojdys
Department of Chemistry & IRIS Adlershof, Humboldt-Universität zu Berlin, Brook-Taylor-Str. 2, 12489 Berlin, Germany
E-mail: liguipin@hu-berlin.de
m.j.bojdys.02@cantab.net

Y. Liu, M. Exner, H. Wang, Dr. K. Scheurell, Dr. J. Huang, Prof. N. Pinna
Department of Chemistry & IRIS Adlershof, Humboldt-Universität zu Berlin, Brook-Taylor-Str. 2, 12489 Berlin, Germany

Dr. T. Schultz, Prof. N. Koch
Humboldt-Universität zu Berlin, Institut für Physik, Institut für Chemie, IRIS Adlershof, Zum Großen Windkanal 2, 12489 Berlin, Germany
and
Helmholtz-Zentrum Berlin, Hahn-Meitner-Platz 1, 14109 Berlin, Germany

Prof. P. Adelhelm
Department of Chemistry & IRIS Adlershof, Humboldt-Universität zu Berlin, Brook-Taylor-Str. 2, 12489 Berlin, Germany
and
Helmholtz-Zentrum Berlin, Hahn-Meitner-Platz 1, 14109 Berlin, Germany

Dr. R. Muydinov
Institute for Semiconductor- and High-Frequency-System Technologies, Technische Universität Berlin, Einsteinufer 25, 10587 Berlin, Germany

Dr. P. Szymoniak
Bundesanstalt für Materialforschung und-prüfung (BAM), Unter den Eichen 87, 12205 Berlin, Germany

© 2024 The Authors. Angewandte Chemie International Edition published by Wiley-VCH GmbH. This is an open access article under the terms of the Creative Commons Attribution License, which permits use, distribution and reproduction in any medium, provided the original work is properly cited.

© 2024 The Authors. Angewandte Chemie International Edition published by Wiley-VCH GmbH

result in low utilization of active material, fast capacity fading and short cycling life.[6]

To tackle such issues, researchers have dedicated lots of efforts including fabricating the high-electrical conductivity cathode with confinement effect and/ or strong affinity towards lithium polysulfides,[7] modifying the separator with lithium polysulfides-blocking characteristics,[8] exploring novel electrolyte and creating hybrid anode without lithium dendrites growth and dead sulfur deposition.[9] Among these approaches, a superior cathode design was considered to be most effective to mitigate the shuttle problem from the cradle. Different materials such as templated carbon nanotubes, cages or graphene-based structures, metal–organic frameworks and porous organic polymers have been prepared to play a role as sulfur host materials,[10] which control the distribution of active sulfur in electrode, and finally to chemically or physically absorb the lithium polysulfides during cycling.[11]

Recently, porous organic polymers have emerged as promising candidates for designing Li–S cathodes, primarily due to their exceptional porosity characteristics and remarkable electrochemical stability.[12] Moreover, they offer the advantage of easy controllability, allowing for the introduction of specific functional groups like nitrogen (N) and oxygen (O) into the polymer network. These functional groups exhibit strong binding energies with sulfur species, effectively preventing the escape of lithium polysulfides. This property is highly beneficial for enhancing the overall performance and durability of Li–S batteries. However, the traditional preparation processes of these cathodes were complex, usual the flows are as follow: i) synthesizing the target polymer under harsh conditions, such as high temperature and inert atmosphere; ii) using lots of solvent washing and purifying the former product; iii) creating a polymer/S composition by means of sulfur melting or dissolving diffusion; iv) combining the polymer/S composite with conductive carbon additive and binder to prepare a slurry for coating on current collector surface. Take into consideration of above process flows are time and energy consuming, it facing big challenges when it goes into real scale-up industrial fabricating.[13] On another hand, the use of additional binder in slurry preparation would lower the electrical conductivity of the whole electrode.[14] What's more, the gravimetric energy density of Li–S cells was reduced, as additional binders typically account for at least 10 % of the electrode weight. Hence, the pursuit of a binder-free cathode, combining the advantages of porous polymer and carbon material while maintaining an uncomplicated and straightforward fabrication process was anticipated to achieve greatly improved performance of Li–S batteries.

In this work, we designed a novel imine polymer@KB/S cathode based on a one-pot, in situ polymerization of imine-based polymer encapsulating Ketjen black/sulfur (KB/S) particles on aluminum surface. The imine polymer matrix was initiated with a small amount of acetic acid (0.05 M). The covalent bonds of the polymer network matrix improve the mechanical and chemical strength of our cathode. The presence of a continuous π-conjugated backbone in the imine-based polymer significantly enhances electron transport, facilitating the flow of electrons from the highly insulating sulfur active material to the current collector. In summary, the imine-based covalent polymer networks matrix acts at the same time as (i) a strong networked binder connecting KB/S NPs to form a film integrity, as (ii) a semi-permeable membrane that enables transport of ions and electrolyte, and as (iii) a robust host to trap the soluble polysulfides and alleviate the "shuttle effect". This facile method yields cathodes (imine-polymer@KB/S) of superior performance and remarkable capacity retention.

Results and Discussion

Structural Characterization of TAPB-TA Film and TAPB-TA@KB/S Electrode

The imine polymer was based on Schiff-base condensation, a dynamic covalent coupling reaction between an amine (1,3,5-tris(4-aminophenyl)benzene, TAPB) and an aldehyde (Terephthalaldehyde, TA)), enabling the formation of a conjugated imine bond (Figure 1a).[15] A yellow, homogeneous imine polymer film (Figure S1) can be obtained on an aluminum surface with a small amount of acetic acid as a triggering agent. Thermo gravity analysis (TGA) shows there is almost no mass loss below 150 °C (Figure S2) and the DSC results of polyimine showed high glass transition temperatures (Tg) to be close to 300 °C (Figure S3). The polyimine were demonstrated to be amorphous by PXRD results (Figure S4). The electrochemical tolerance was also tested by adopting a neat TAPB-TA film with lithium metal as counter electrode, to run a cyclic voltammetry (CV) at a scan rate of 0.01 $mV S^{-1}$ between 1.6 and 3.0 V (vs. Li/Li^{+}) (Figure S5). No redox signals were detected demonstrates that the TAPB-TA is inert under this voltage window of Li–S battery. As mentioned above, the TAPB-TA polymer fabricated under mild conditions owns good physical and chemical stability, indicating a promising potential to Li–S battery. The cathode of TAPB-TA@KB/S are prepared by blending the two monomers precursors solution with KB/S particles (which with a sulfur ratio of ~65 %, Figure S6), and then the slurry was directly coated on the current collector surface. The polymerization was driven to completion with a higher temperature (60 °C) vacuum baking, and eventually the solvent NMP and residue acid were removed.

To gain insight into the chemical bonds and definite structure, the neat TAPB-TA film and TAPB-TA@KB/S have been fully characterized using Fourier transform infrared (FT-IR), Solid state Raman, X-ray photoelectron spectroscopy (XPS) and ^{13}C CP-MAS NMR measurements. As shown in Figure 1b, the feature peak originating from the imine bonds (C=N) (~1590 cm^{-1}) in both of neat TAPB-TA film and TAPB-TA@KB/S from the FT-IR spectrum confirmed the completion of the Schiff base reaction.[16] An FT-IR spectrum (Figure S7) of neat TAPB-TA polymer powder which synthesized by solution strategy with a high acid concentration (1.2 M) was given to further comparing with TAPB-TA@KB/S electrode, which demonstrated a high completion of in situ polymerization during electrode

© 2024 The Authors. Angewandte Chemie International Edition published by Wiley-VCH GmbH

15213773, 2024, 28, Downloaded from https://onlinelibrary.wiley.com/doi/10.1002/anie.202400382 by Humboldt-Universitat Zu Berlin, Wiley Online Library on [06/01/2025]. See the Terms and Conditions (https://onlinelibrary.wiley.com/terms-and-conditions) on Wiley Online Library for rules of use; OA articles are governed by the applicable Creative Commons License

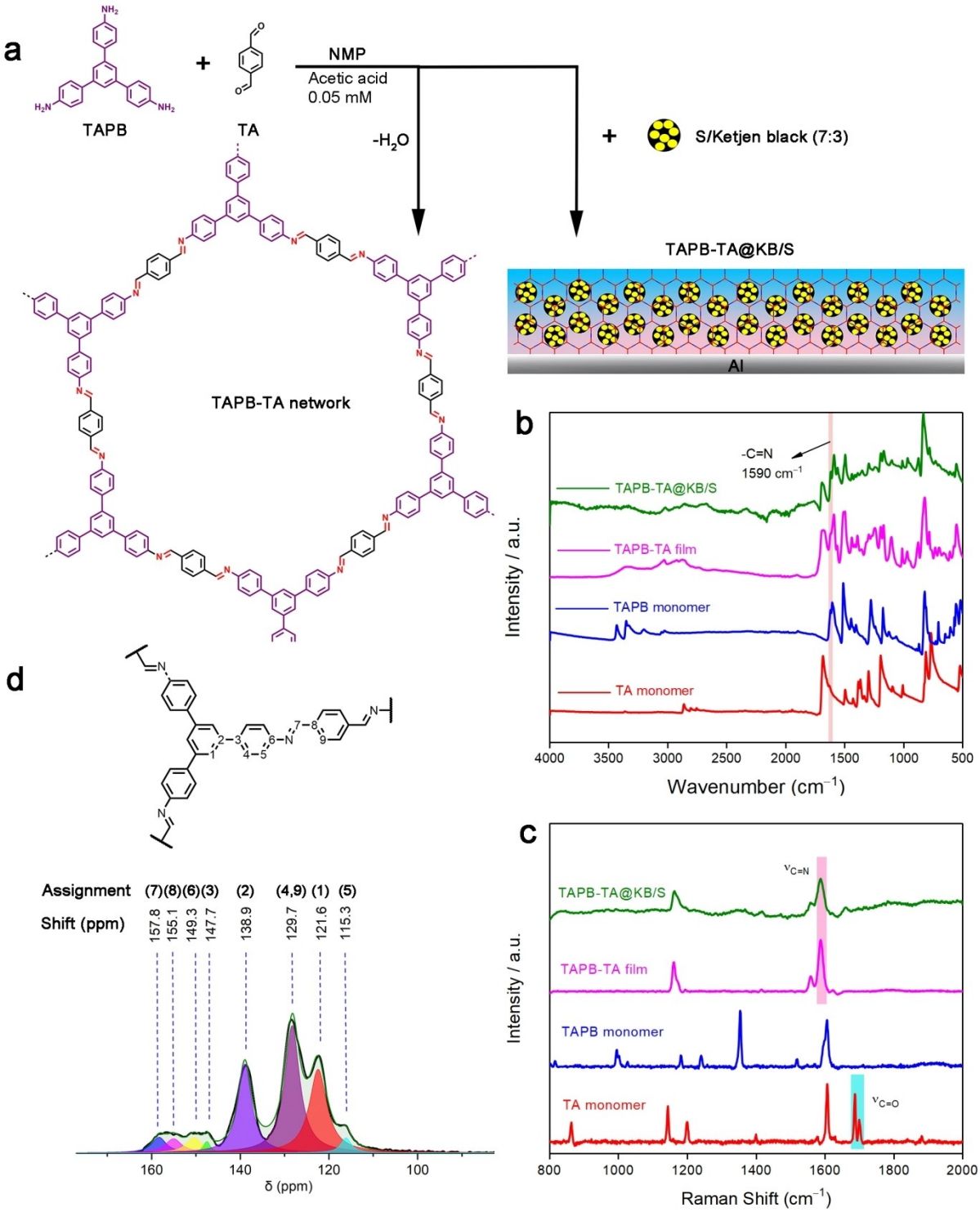

Figure 1. (**a**) Reaction Scheme for the TAPB-TA polymer network and the fabrication of TAPB-TA@KB/S electrodes. (**b**) The FT-IR spectrum of TAPB-TA@KB/S, TAPB-TA polymer film and the monomers, respectively. (**c**) The Raman spectra of TAPB-TA@KB/S, TAPB-TA polymer film and the monomers, with fluorescence background collected with a 532 nm laser. (**d**) ^{13}C cross-polarization/magic-angle-spinning (CP/MAS) solid-state NMR spectrum of the TAPB-TA polymer film.

fabricating. The Raman spectra (Figure 1c) provide further information of chemical bonds of NH_2, HC=O and C=N groups. The bands at 1687 and 1700 cm^{-1} correspond to the aldehyde C=O stretching vibrations, as well as the band located at 1353 cm^{-1} in the spectra of amine TAPB attribute to a stretching vibration of β-ring and wagging of its NH_2 group.[15–16] The intensity of these bands were significantly reduced in the spectra of the TAPB-TA film, as well as in

© 2024 The Authors. Angewandte Chemie International Edition published by Wiley-VCH GmbH

15213773, 2024, 28, Downloaded from https://onlinelibrary.wiley.com/doi/10.1002/anie.202400382 by Humboldt-Universitat Zu Berlin, Wiley Online Library on [06/01/2025]. See the Terms and Conditions (https://onlinelibrary.wiley.com/terms-and-conditions) on Wiley Online Library for rules of use; OA articles are governed by the applicable Creative Commons License

the spectra of TAPB-TA@KB/S electrode. Meanwhile, the obvious peaks around 1560 cm^{-1} (1558 cm^{-1} and 1587 cm^{-1}) in TAPB-TA@KB/S and TAPB-TA film corresponded to stretching vibrations of the newly formed C=N bonds. The effective formation of imine linkage was further confirmed by ^{13}C NMR spectroscopy and X-ray Photoelectron Spectroscopy (XPS). A peak at approximately 158 ppm was observed in TAPB-TA film attribute to C atoms in the C=N linkage (Figure 1d).[16] The ssNMR spectra (Figure S8) and XPS spectra (Figure S9) of TAPB-TA@KB/S electrode give the information of elemental environments, which indicating a high condensation rate of polymer film by this process. In summary, these spectroscopic analyses confirmed the formation of a conjugated imine polymer network around KB/S particles in the electrode.

Scanning electron microscopy (SEM) images were taken to reveal the microstructure of the pristine TAPB-TA@KB/S electrodes. The electrode surface of TAPB-TA@KB/S is smooth and with some small cracks and voids which could facilitate electrolyte wetting and lead to higher sulfur utilization (Figure 2a). More detailed elemental information of the surface was given by EDX (Figure S10). In contrast, the cathode fabricated via polyvinylidene difluoride (PVDF) contains many large cracks (Figure S11). This is attributed to i) its high crystallinity, and ii) the high-viscosity slurry, which tends to preserve its original thickness during drying process.[17] SEM at higher magnifications showed that TAPB-TA@KB/S exhibits a porous, sponge-like structure (Figure 2b). From transmission electron microscopy (TEM) spectra (Figure S12), the TAPB-TA coated KB/S particles could be observed with a diameter around 30–40 nm. Cross-section SEM imaging (Figure 2c) shows TAPB-TA@KB/S with a thickness of approximately 50 μm, adhering firmly to the aluminum surface without noticeable gap. The elemental mapping for the cross-section confirms the homogeneous distribution of carbon (C), nitrogen (N), and sulfur (S), supporting the formation of a uniform cathode (Figure 2d–g).

Electrochemical Performance of Li–S Cells

Electrochemical tests were conducted to assess the battery performance of TAPB-TA@KB/S in half cells with metallic lithium as the counter electrode. For comparison, the cathode PVDF@KB/S was also prepared. In Figure 3a, the columbic efficiencies and cycling curves of TAPB-TA@KB/S and PVDF@KB/S at a discharge rate of 0.2 C are depicted, with 1 C representing 1675 mA g^{-1}. The initial discharge specific capacity of PVDF@KB/S measured to be 1134 mAh g^{-1}, which is lower than the specific capacity of the TAPB-TA@KB/S cathode (1205 mAh g^{-1}). Furthermore, the capacity decay of TAPB-TA@KB/S proves to be notably slower than that of PVDF@KB/S. After 100 cycles, TAPB-TA@KB/S maintained an impressive discharge capacity of 917 mAh g^{-1}, coupled with a remarkable columbic efficiency exceeding 99.5 %. In contrast, PVDF@KB/S displayed a lower capacity of 774 mAh g^{-1} after 100 cycles. Moreover, a significant drop in columbic efficiency was observed with PVDF binder, which would lead a more rapid decline in performance as the cycling continued. The TAPB-TA@KB/S cathode exhibited superior rate performance, as displayed in Figure 3b. At 3 C, it retained a remarkable capacity of 807 mAh g^{-1}. Additionally, the TAPB-TA@KB/S cathode shows excellent capacity recovery during a transition from 3 C to 0.5 C, conserving 98.7 % of its original capacity. The charge–discharge behaviors of the two distinct cathodes were investigated, as illustrated in Figure 3c. In comparison

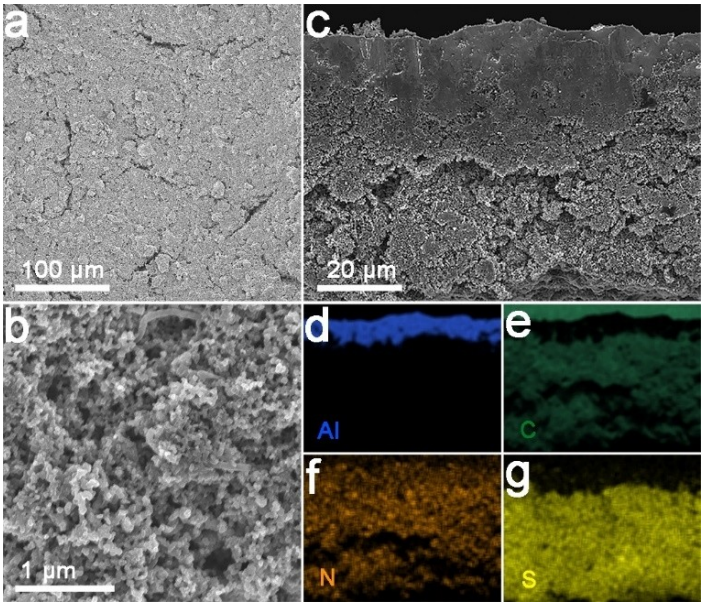

Figure 2. Scanning electron microscopy (SEM) images showing (**a**) the top-view electrode surface and (**b**) the morphology of the composition in electrodes. (**c**) Cross-section morphology of TAPB-TA@KB/S electrode. (**d**, **e**, **f**, **g**) Elemental mapping images showing the homogeneous distribution of polymer and active sulfur.

© 2024 The Authors. Angewandte Chemie International Edition published by Wiley-VCH GmbH

15213773, 2024, 28, Downloaded from https://onlinelibrary.wiley.com/doi/10.1002/anie.202400382 by Humboldt-Universitat Zu Berlin, Wiley Online Library on [06/01/2025]. See the Terms and Conditions (https://onlinelibrary.wiley.com/terms-and-conditions) on Wiley Online Library for rules of use; OA articles are governed by the applicable Creative Commons License

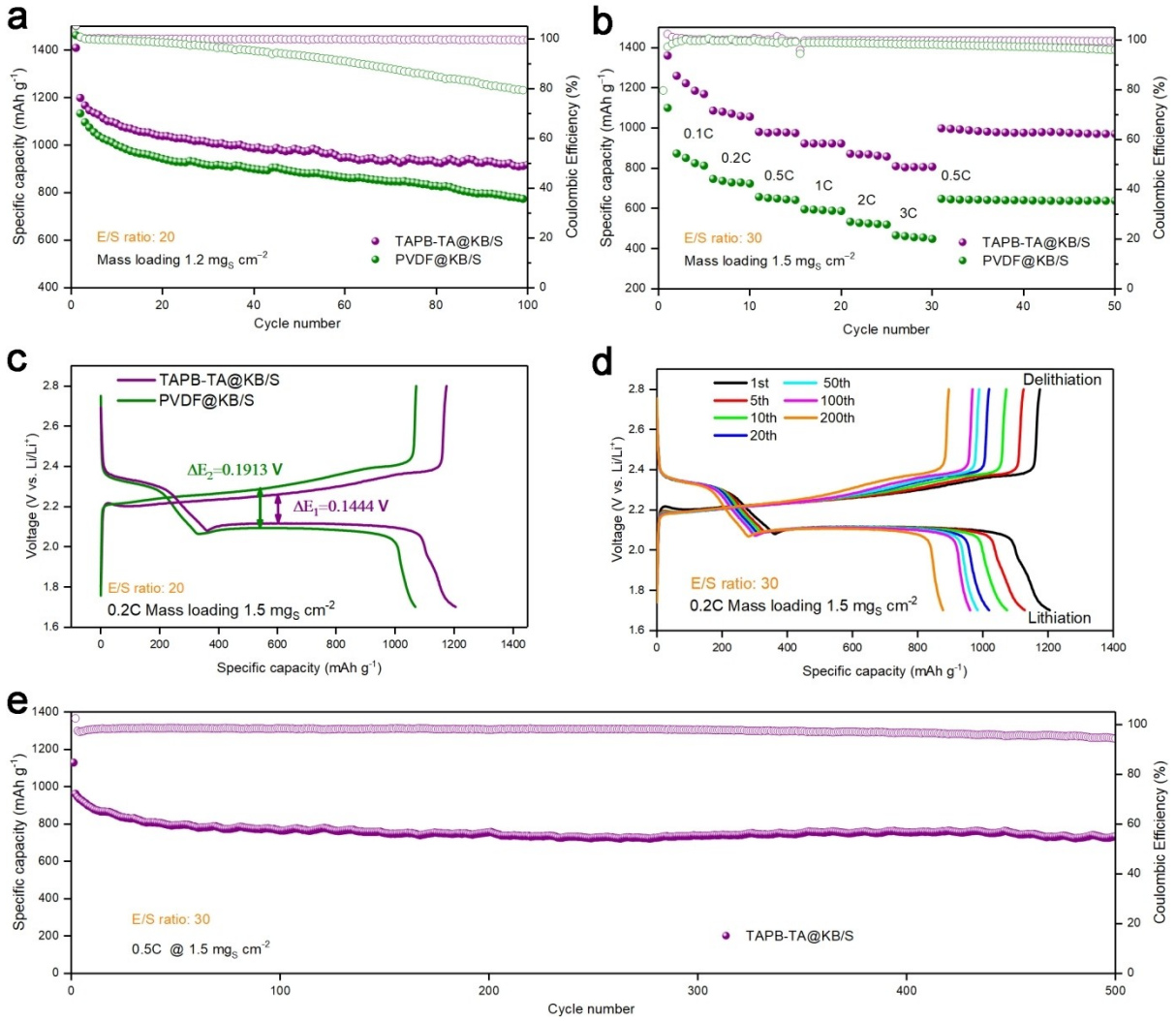

Figure 3. (**a**) Cycling performance of the TAPB-TA@KB/S (in purple) and compared to electrodes using conventional binder PVDF@KB/S (in green) cathode. Both electrodes were cycled at C/2, including the initial one pre-cycle at 0.05 C within a voltage window of 1.7–2.8 V vs. Li^+/Li. (**b**) Rate performance of the TAPB-TA@KB/S and PVDF@KB/S conducted with different current density. (**c**) Voltage profiles of the first cycle of TAPB-TA@KB/S and PVDF@KB/S cathodes at 0.2 C. (**d**) Voltage profiles of different cycles of TAPB-TA@KB/S cathode (**e**) Long-term cycling performance of the TAPB-TA@KB/S at 0.5 C.

to the PVDF cathode, TAPB-TA@KB/S presents an elevated discharge plateau and a lower charge plateau ($\Delta E_2 < \Delta E_1$), indicating a reduced polarization. In the initial cycle, the energy density calculated based on monolayer of TAPB-TA@KB/S electrode (2569 Wh kg^{-1}) was ~13.8 % higher than that of PVDF@KB/S (2257 Wh kg^{-1}). Notably, the TAPB-TA@KB/S cathode owns a higher sulfur utilization (71.5 %) in contrast to PVDF@KB/S (64.8 %), while simultaneously maintaining a consistent and lower polarization even after 100 cycles (depicted in Figure 3d). During extended 500 cycles testing at a current of 0.5 C, the TAPB-TA@KB/S cathode displays minimal capacity decay (0.11 % per cycle) after 500 cycles (Figure 3e). Different electrodes after 100 cycles were dissembled and without washing (Figure S13). The electrode with PVDF has a very severe sulfur shuttle which exhibited a dark brown color, while the electrode with TAPB-TA showed a lighter yellowish which means less sulfur species migrated out. And with less amount electrolyte injection, the shuttle effect also got decreased. In summary, the Li–S cell featuring the TAPB-TA polymer exhibits excellent electrochemical properties (i.e., specific capacities, rate capability and cycling stabilities), which is very competitive with many organic and inorganic host materials. (Table S1) We carried out a cost assessment for the practical fabrication of electrodes using this technology in the lab based on the list prices of fine chemical suppliers (Table S2). This analysis showed that the TAPB monomer is the main cost driver, accounting for over 80 % of the total cost. However, scaling up the production of this monomer through a reliable supplier could potentially mitigate this cost issue, making the technology more economically viable.

© 2024 The Authors. Angewandte Chemie International Edition published by Wiley-VCH GmbH

15213773, 2024, 28, Downloaded from https://onlinelibrary.wiley.com/doi/10.1002/anie.202400382 by Humboldt-Universitat Zu Berlin, Wiley Online Library on [06/01/2025]. See the Terms and Conditions (https://onlinelibrary.wiley.com/terms-and-conditions) on Wiley Online Library for rules of use; OA articles are governed by the applicable Creative Commons License

Evolution of the Composition and Morphology of Sulfur-Polymer Electrodes

Due to the essential role of a stable interfacial layer in ensuring the fast kinetics and superior rate capacity of Li–S cells, an in-depth analysis of surface components and relevant chemical bonding was conducted using X-ray photoelectron spectroscopy (XPS). The aim was to investigate the evolution of cathode electrolyte interphase (CEI) species within the electrode across various stages: from the pristine electrode to post-lithiation, post-delithiation, and after 500 cycles of cycling. Figure 4a(I) depicts the S2p binding energy of both pristine and cycled sulfur electrodes within a DOL/DME electrolyte. Specifically, the S2p peaks at 163.9 and 165.1 eV are distinctive indicators of S–S bonds associated with elemental S_8 present in the pristine cathode.[18] Following the initial discharge (Figure 4a(II)), the S–S peak persists a subdued intensity, accompanied by the emergence of new peaks at lower energies (162.7 eV and 163.9 eV, corresponding to Li_2S_2, and 161.0 eV and 162.2 eV, corresponding to Li_2S).[19] This observation confirms the transformation of elemental S into S^{2-} through electrochemical reduction, leading to the generation of discharge products such as Li_2S or Li_2S_2. Notably, these peaks nearly disappeared in the fully charged state (Figure 4(III)), indicating the significantly reversible nature of this process. This inherent reversibility underpins the exceptional specific capacity and columbic efficiency of the TAPB-TA@KB/S cell. In contrast, for the electrodes within the PVDF@KB/S–Li cell, discernible variations in the S2p peaks were

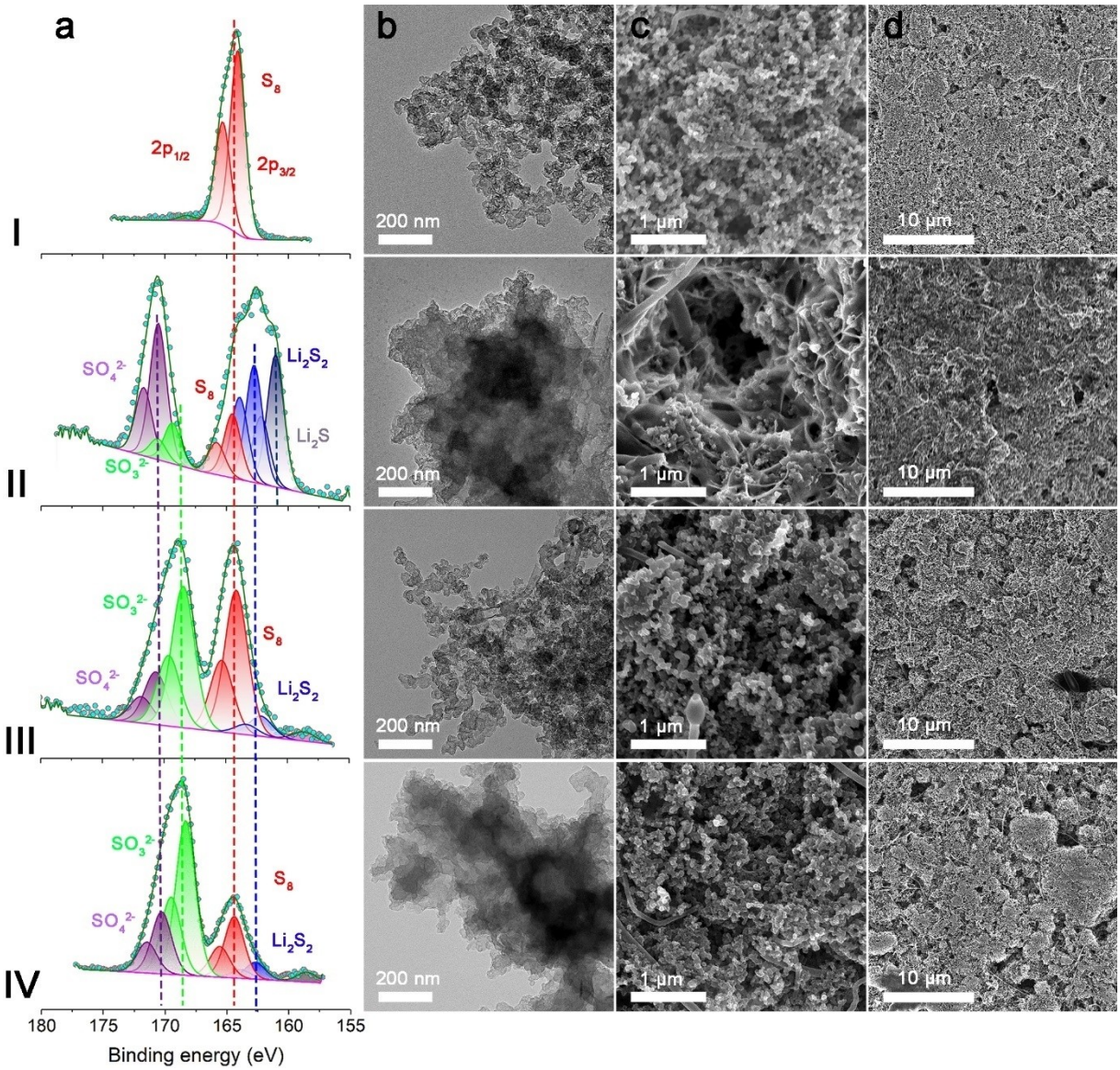

Figure 4. Characterization of TAPB-TA@KB/S electrodes using (**a**) X-ray photoelectron spectroscopy (XPS) data from the S2p region, (**b**) transmission electron microscopy (TEM), and (**c, d**) scanning electron microscopy (SEM) at different magnification. Data are presented for TAPB-TA@KB/S electrodes in the pristine state (**I**), after the first lithiation (**II**), after the first delithiation (**III**), and after the 500th delithiation (**IV**). Cycling was performed using constant current mode for at C/2 within a voltage range of 1.7–2.8 V versus Li/Li^+.

© 2024 The Authors. Angewandte Chemie International Edition published by Wiley-VCH GmbH

15213773, 2024, 28, Downloaded from https://onlinelibrary.wiley.com/doi/10.1002/anie.202400382 by Humboldt-Universitat Zu Berlin, Wiley Online Library on [06/01/2025]. See the Terms and Conditions (https://onlinelibrary.wiley.com/terms-and-conditions) on Wiley Online Library for rules of use; OA articles are governed by the applicable Creative Commons License

observed: i) the initial strong intensity of pristine S–S peaks persisted (Figure S14a(I)); ii) the primary lithiated product in the fully discharged state was Li_2S_2, with a weak Li_2S signal being discernible (Figure S14a(II)); iii) post full charging, the peaks at 162.2 eV and 163.6 eV associated with Li_2S_2 remained prominent (Figure S14a(III)). These distinctions collectively suggest an inadequate conversion of sulfur within the PVDF@KB/S–Li cell, ultimately contributing to a lower initial capacity when compared to the TAPB-TA@KB/S–Li cell. In the PVDF@KB/S–Li cell, notable peaks of Li_2S and Li_2S_2 were observed during the charging state after 500 cycles (Figure S14a(IV)). Conversely, the lower oxidation S2p peaks for Li_2S_2 and Li_2S were consistently present throughout the cycling process and exhibited accumulation over cycles in the TAPB-TA@KB/S cell (Figure 4a(IV)). This phenomenon signifies the sustained electrochemical reversibility as the cycling depth increases for the cell. This observation aligns harmoniously with the observed enhancements in specific capacity and capacity retention for the TAPB-TA@KB/S-Li cell. Moreover, an analysis of the Li_2SO_x species present within the CEI was conducted for both electrodes. Notably, the intensities of Li_2SO_4 (at 170.8 eV and 171.9 eV) and Li_2SO_3 (at 168.4 eV and 169.6 eV) remained consistently stable in the TAPB-TA@KB/S electrode.[20] Starting from the initial discharging step, the presence of Li_2SO_3 and Li_2SO_4 was detectable. In contrast, within the PVDF@KB/S electrode, a lower intensity of Li_2SO_x was observed during the initial discharging process, and there were no recognizable peaks corresponding to Li_2SO_3 initially. These findings demonstrated an earlier development of a more robust CEI in the TAPB-TA@KB/S electrode.

The XPS spectra of C1s, N1s, and F1s from TAPB-TA@KB/S cathodes across various charge and discharge cycles are presented in Figure S15 and Table S3, offering a comprehensive insight into the CEI components. In the pristine cathode (Figure S15(I)), the C1s peak at 284.8 eV corresponds to the imine structure's C–C and C=C bonds, while the peaks at 286.1 eV are attributed to C=N bonds.[21] After 1st lithiation (Figure S15(II)), the emergence of new species (C=O and C–O resulting from $ROCO_2Li$ and Li_2CO_3, respectively, located at 288.0 eV and 290.1 eV) covered the original C1s signal. Additionally, a peak at 291.5 eV signifies the presence of C–F bonds, which stems from the decomposition of electrolyte components.[22] Remarkably, throughout subsequent charge and extended cycling processes, the C=O and C–F (CF_2) peaks maintain both high intensity and consistent ratios, indicating a stable CEI (Figure S15a(II), a(III) and a(IV)). In the N1s spectra, the 400.1 eV peak corresponds to Li–N bonds stemming from Li_3N (Figure S15b(II)).[23] The F1s spectra revealed a rich LiF was formed following complete charging (Figure S15c). This LiF-rich CEI also contributes to enhanced columbic efficiency and capacity retention.

Ex situ TEM and SEM imaging of TAPB-TA@KB/S and PVDF@KB/S electrodes at different cycling stages (Figure 4b–d and Figure S14b–c) were conducted to investigate the morphological changes. As shown in Figure 4b(I), the TAPB-TA polymer acts as a binder effectively joining KB/S NPs to form a porous imine@KB/S composite. After the first lithiation, the surface of cathode was uniformly deposited with discharge products, which comprise of insoluble lithium sulfides (Li_2S and/or Li_2S_2). These flakes were reassembled into structures like nano walls. Following a full charging cycle, these nano walls disappeared fully, indicating a nearly complete transformation of the lithium sulfides back to sulfur, which then trapped within the porous structure. Impressively, even after 500 cycles, TAPB-TA@KB/S displays no evident lithium sulfide flakes. These results suggested a good reversibility during long-term cycling. In contrast, large lithium sulfides aggregations were covered on the surface of PVDF@KB/S (Figure S14b(IV)), which contributed to lower columbic efficiency and reduced specific capacity.

Sulfur Redox Reaction Kinetics and Adsorption of Lithium Polysulfides

The rapid lithium polysulfide redox kinetics at the liquid-solid interface holds crucial importance in achieving high-performance Li–S batteries. Therefore, the Li_2S nucleation behavior in the presence of different binders was investigated using current-time transient spectra, as illustrated in Figure 5a and 5b. Calculated precipitation of Li_2S within the TAPB-TA@KB and PVDF@KB cathodes were 428.1 $mAh\,g^{-1}$ and 244.4 $mAh\,g^{-1}$, respectively. These results validated that the in situ grown TAPB-TA facilitates Li_2S nucleation and deposition. The Li_2S deposition morphologies were characterized by SEM. As depicted in the insets, 3D "flower-like" Li_2S thin flakes were homogeneously deposited on the surface of TAPB-TA@KB. In contrast, uneven distribution and agglomeration of Li_2S particles were observed on PVDF@KB. The densely stacked host material on the surface of PVDF@KB provided fewer nucleation sites and consequently led to a slower nucleation rate.

The diffusion kinetics of the cathodes was analyzed by employing galvanostatic intermittent titration technique (GITT). The discharge/charge curves in Figure 5c and 5d clearly illustrate that the electrode incorporating TAPB-TA polymer exhibited a higher capacity compared to PVDF. Furthermore, the PVDF@KB/S electrode encountered a severe overcharge, which attributed to the shuttle effect. Additionally, the IR drops between the practical operational state and equilibrium of the TAPB-TA@KB/S cathode are comparatively smaller than those observed in PVDF@KB/S (Figure S16a–b). This observation holds true for both the charging and discharging processes, underscoring the enhanced chemical diffusion efficiency of the TAPB-TA polymer. The calculated Li^+ diffusion coefficient ($D_{Li}{}^+$) for TAPB-TA@KB/S ranges from 9.54×10^{-12} to $5.63\times10^{-6}\,cm^2\,s^{-1}$. In contrast, for PVDF@KB/S, the calculated $D_{Li}{}^+$ falls within the range of 3.74×10^{-13} to $6.33\times10^{-8}\,cm^2\,s^{-1}$. These findings align with the results from cyclic voltammetry (CV) measurements of $D_{Li}{}^+$ (Figure S17a–d, Table S4). The higher diffusion coefficients obtained in the TAPB-TA@KB/S cathode facilitate rapid

© 2024 The Authors. Angewandte Chemie International Edition published by Wiley-VCH GmbH

15213773, 2024, 28, Downloaded from https://onlinelibrary.wiley.com/doi/10.1002/anie.202400382 by Humboldt-Universitat Zu Berlin, Wiley Online Library on [06/01/2025]. See the Terms and Conditions (https://onlinelibrary.wiley.com/terms-and-conditions) on Wiley Online Library for rules of use; OA articles are governed by the applicable Creative Commons License

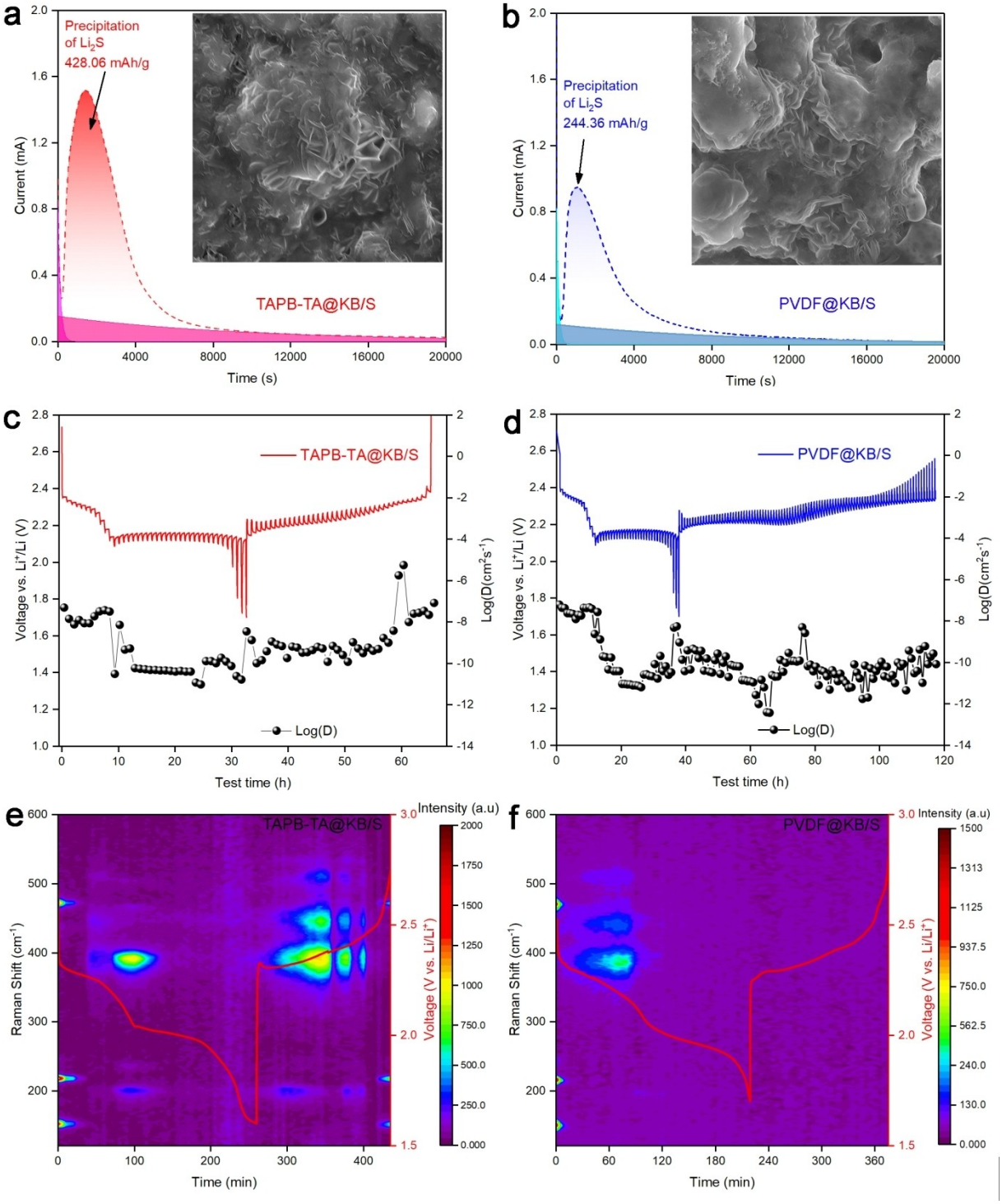

Figure 5. (**a**) and (**b**) Redox reaction kinetics and the Li_2S nucleation performance of TAPB-TA@KB/S and PVDF@KB/S, insets are Li_2S deposition morphologies. (**c**) and (**d**) GITT curves with corresponding lithium ion diffusion co-efficient of different electrodes with TAPB-TA and PVDF, respectively. (**e**) and (**f**) corresponding to two-dimensional (2D) time-resolved Raman spectra of TAPB-TA@KB/S and PVDF@KB/S, respectively.

Li^+ transport, ultimately enhancing the rate capability of the battery.

Lithium polysulfide conversions were monitored using Li_2S_6 symmetrical battery. As depicted in Figure S18, the curve associated with the TAPB-TA polymer qualitatively shows heightened redox peaks in comparison to PVDF. This observation confirms the notably enhanced conversion between Li_2S_6 and Li_2S within TAPB-TA@KB/S cathode. This outcome can be attributed to TAPB-TA's superior lithium polysulfide adsorption capacity, which effectively

© 2024 The Authors. Angewandte Chemie International Edition published by Wiley-VCH GmbH

15213773, 2024, 28, Downloaded from https://onlinelibrary.wiley.com/doi/10.1002/anie.202400382 by Humboldt-Universitat Zu Berlin, Wiley Online Library on [06/01/2025]. See the Terms and Conditions (https://onlinelibrary.wiley.com/terms-and-conditions) on Wiley Online Library for rules of use; OA articles are governed by the applicable Creative Commons License

accelerates lithium polysulfide redox kinetics. As depicted in Figure S19, the lithium polysulfide adsorption of these two electrodes material was conducted directly. The color of Li_2S_6 solution vanished with TAPB-TA@KB/S, while it retained a brownish color with PVDF@KB/S. Different absorbance intensity of lithium polysulfide at around 430 nm in UV/Vis gave more clear evidence.[24] Furthermore, DFT calculation was performed as an efficient way to elucidate the chemical interaction between sulfur species and the TAPB-TA polymer as well the PVDF binder (Figure S20a–b). Consistent with the adsorption test, the Li_2S_6 adsorption energy of TAPB-TA (−4.882 eV) is much higher than that of PVDF (−0.2414 eV). The adsorption energy of soluble lithium polysulfides (Li_2S_4 and Li_2S_6, Li_2S_8) as well as insoluble products (S_8 and Li_2S) with TAPB-TA displayed higher than that with PVDF, which attributed to rich anchoring site provided by imine bond and 2D network facilitating the interaction.[13b] While in the linear chain structure of PVDF, the highly electronegative fluorine atoms may induce strong repulsion with sulfur atoms. This explains why PVDF_S_8 exhibits positive absorption energy, indicating a lack of absorbing behavior. The polysulfides retention also tested by self-discharge (Figure S21). The battery with TAPB-TA remained stable for more than 1300 hours, originating from the great lithium polysulfide adsorption and shuttle effect alleviation.

The electron and charge transport characteristics within the cathodes were investigated using electrochemical impedance spectroscopy (EIS) (Figure S22 and Table S5). As shown in the Nyquist plots, the diameter of the semicircle in the high-frequency region is assigned to charge transfer resistance, which consists of the intrinsic electron resistance R_s of the electrodes and the charge-transfer resistance R_{ct}, while in the low-frequency region the sloping line corresponds to Warburg impendence W_0 related to mass diffusion in the electrolyte.[25] Notably, the intrinsic electron resistance R_s exhibited a similarity for both electrodes. While, the R_{ct} value of the TAPB-TA@KB/S electrode is obviously lower than that of PVDF@KB/S cathode. This reduction can primarily be attributed to the uniform voids/pores present in the TAPB-TA@KB/S cathode. These voids/pores facilitate robust contact between the electrolyte and the active material, thus enabling rapid electrochemical lithium polysulfides redox kinetics and efficient electron/ion transportation.

Operando Raman spectroscopy was employed to monitor species conversion (Figure S23a).[26] The Raman curves of the Li–S battery with TAPB-TA polymer and PVDF binder at different voltage stages are presented (Figure S23b and 23c). In OCV stage, the peaks at 150, 219, and 475 cm^{-1} can be attributed to initial S_8.[27] During the first discharge plateau, negligible peaks around 398 cm^{-1} emerged, indicating the formation of long-chain polysulfide Li_2S_6.[28] Simultaneously, a peak appeared at around 198 cm^{-1} suggesting the immediate formation of Li_2S_4. As the voltage decreases, the signals associated with polysulfides rapidly diminish, indicating a conversion to short-chain products. Conversely, as the cell charged (below 2.4 V), the signals of Li_2S_4 and polysulfide Li_2S_6 reappeared in TAPB-TA@KB/S due to the oxidation of low-order polysulfides (Li_2S_2, Li_2S) into high-order polysulfides. Subsequently, as the voltage increases, the polysulfide compounds disappear, and peaks at the same locations as S_8 re-emerged with strong intensity. While in PVDF@KB/S, it hard to detect the signals of sulfur species during charging process. And after the following fully lithiation, there's no S_8 signal, which could be ascribed to the loss of active sulfur. In addition, we conducted operando optical microscopy to gain insights into the behavior of sulfur/sulfide species in operando. Cells assembled with a PVDF@KB/S electrode showed significant sulfur shuttling, as evidenced by a brownish colored separator (Video S1). In contrast, the cell with a TAPB-TA@KBS electrode showed only a pale yellowish coloration of the separator, indicating superior sulfur retention (Video S2). The improved retention of sulfur/sulfide was maintained even with a thick electrode (3.5 $mg_s cm^{-2}$), highlighting the importance of the polyimine-network for battery performance (Video S3). These findings underscore the beneficial effects of the TAPB-TA polymer binder in facilitating lithium polysulfides adsorption and Li^+ transport, thereby enhancing the sulfur redox reaction kinetics for high and stable battery performance.

Conclusion

In summary, a one-pot, in situ growth strategy has been successfully employed to fabricate an imine polymer encapsulated sulfur-based electrode. The electrode shows a remarkable capacity, exceptional rate performance, and superior long-term stability due to the conjugated porous polymer that surrounds the active material, sulfur/Li_2S. DFT calculations and operando Raman further elucidated that the imine group on the surface significantly enhances the affinity with polysulfides, thereby contributing to an overall performance enhancement and an inhibition of the "sulfur-shuttle" effect. We anticipate that in situ growth of conjugate polymers as the binder and facilitator of charge- and mass-transport will expedite the practical applications of sulfur-based high energy density batteries.

Acknowledgements

We thank Mr. Christoph Erdmann for TEM measurements, Tobias Heinemann for SEM measurements, Christian Heinekamp for TGA measurements, Yanchen Liu for experiments discussion. G.L. acknowledges the fellowship from the China Scholarship Council (CSC). This work was funded by the Feder Ministry of Education and Research (BMBF) T!Raum—TransferRäume für die Zukunft von Regionen" GreenCHEM and the European Research Council (ERC) Proof of Concept Grant Scheme (LiAnMat-957534). Open Access funding enabled and organized by Projekt DEAL.

© 2024 The Authors. Angewandte Chemie International Edition published by Wiley-VCH GmbH

15213773, 2024, 28, Downloaded from https://onlinelibrary.wiley.com/doi/10.1002/anie.202400382 by Humboldt-Universitat Zu Berlin, Wiley Online Library on [06/01/2025]. See the Terms and Conditions (https://onlinelibrary.wiley.com/terms-and-conditions) on Wiley Online Library for rules of use; OA articles are governed by the applicable Creative Commons License

Conflict of Interest

The authors declare no conflict of interest.

Data Availability Statement

The data that support the findings of this study are openly available in Zenodo at https://doi.org/10.5281/zenodo.10465504, reference number 10465504.

Keywords: imine polymer · in situ growth · cathode · lithium sulfur batteries

[1] M. Armand, J. M. Tarascon, *Nature* **2008**, *451*, 652–657.
[2] a) K. Mizushima, P. C. Jones, P. J. Wiseman, J. B. Goodenough, *Mater. Res. Bull.* **1980**, *15*, 783–789; b) A. Yamada, S. C. Chung, K. Hinokuma, *J. Electrochem. Soc.* **2001**, *148*, A224.
[3] a) M. Park, J. Ryu, W. Wang, J. Cho, *Nat. Rev. Mater.* **2016**, *2*, 16080; b) J. W. Choi, D. Aurbach, *Nat. Rev. Mater.* **2016**, *1*, 16013.
[4] R. Fang, S. Zhao, Z. Sun, D.-W. Wang, H.-M. Cheng, F. Li, *Adv. Mater.* **2017**, *29*, 1606823.
[5] T. Lee, P. T. Dirlam, J. T. Njardarson, R. S. Glass, J. Pyun, *J. Am. Chem. Soc.* **2022**, *144*, 5–22.
[6] a) Y. Chen, T. Wang, H. Tian, D. Su, Q. Zhang, G. Wang, *Adv. Mater.* **2021**, *33*, 2003666; b) Z. Wei Seh, W. Li, J. J. Cha, G. Zheng, Y. Yang, M. T. McDowell, P.-C. Hsu, Y. Cui, *Nat. Commun.* **2013**, *4*, 1331.
[7] a) X. Ji, K. T. Lee, L. F. Nazar, *Nat. Mater.* **2009**, *8*, 500–506; b) N. Jayaprakash, J. Shen, S. S. Moganty, A. Corona, L. A. Archer, *Angew. Chem. Int. Ed.* **2011**, *50*, 5904–5908.
[8] a) J.-Q. Huang, Q. Zhang, F. Wei, *Energy Storage Mater.* **2015**, *1*, 127–145; b) Y. Xiang, J. Li, J. Lei, D. Liu, Z. Xie, D. Qu, K. Li, T. Deng, H. Tang, *ChemSusChem* **2016**, *9*, 3023–3039.
[9] a) S. Zhang, K. Ueno, K. Dokko, M. Watanabe, *Adv. Energy Mater.* **2015**, *5*, 1500117; b) J. Huang, A. Martin, A. Urbanski, R. Kulkarni, P. Amsalem, M. Exner, G. Li, J. Müller, D. Burmeister, N. Koch, T. Brezesinski, N. Pinna, P. Uhlmann, M. J. Bojdys, *Nat. Sci.* **2022**, *2*, e20210105; c) S.-H. Chung, A. Manthiram, *Adv. Mater.* **2018**, *30*, 1705951; d) C. V. Amanchukwu, *Joule* **2020**, *4*, 281–285.
[10] a) R. Fang, K. Chen, L. Yin, Z. Sun, F. Li, H.-M. Cheng, *Adv. Mater.* **2019**, *31*, 1800863; b) X. Wang, C. Zhao, B. Liu, S. Zhao, Y. Zhang, L. Qian, Z. Chen, J. Wang, X. Wang, Z. Chen, *Adv. Energy Mater.* **2022**, *12*, 2201960.
[11] a) D. Luo, M. Li, Q. Ma, G. Wen, H. Dou, B. Ren, Y. Liu, X. Wang, L. Shui, Z. Chen, *Chem. Soc. Rev.* **2022**, *51*, 2917–2938; b) Q. Zhang, Q. Huang, S.-M. Hao, S. Deng, Q. He, Z. Lin, Y. Yang, *Adv. Sci.* **2022**, *9*, 2103798.
[12] a) K. Liu, H. Zhao, D. Ye, J. Zhang, *Chem. Eng. J.* **2021**, *417*, 129309; b) Z. Cheng, H. Pan, H. Zhong, Z. Xiao, X. Li, R. Wang, *Adv. Funct. Mater.* **2018**, *28*, 1707597.
[13] a) J. Jin, W. Cai, J. Cai, Y. Shao, Y. Song, Z. Xia, Q. Zhang, J. Sun, *J. Mater. Chem. A* **2020**, *8*, 3027–3034; b) H. Duan, K. Li, M. Xie, J.-M. Chen, H.-G. Zhou, X. Wu, G.-H. Ning, A. I. Cooper, D. Li, *J. Am. Chem. Soc.* **2021**, *143*, 19446–19453; c) Y. Ge, J. Li, Y. Meng, D. Xiao, *Nano Energy* **2023**, *109*, 108297; d) X.-F. Liu, H. Chen, R. Wang, S.-Q. Zang, T. C. W. Mak, *Small* **2020**, *16*, 2002932.
[14] A. Kraytsberg, Y. Ein-Eli, *Adv. Energy Mater.* **2016**, *6*, 1600655.
[15] W. Dai, F. Shao, J. Szczerbinski, R. McCaffrey, R. Zenobi, Y. Jin, A. D. Schluter, W. Zhang, *Angew. Chem. Int. Ed. Engl.* **2016**, *55*, 213–217.
[16] C. Li, D. Li, W. Zhang, H. Li, G. Yu, *Angew. Chem. Int. Ed. Engl.* **2021**, *60*, 27135–27143.
[17] M. Li, J. Zhang, Y. Gao, X. Wang, Y. Zhang, S. Zhang, *J. Mater. Chem. A* **2021**, *9*, 2375–2384.
[18] X. Song, D. Tian, Y. Qiu, X. Sun, B. Jiang, C. Zhao, Y. Zhang, L. Fan, N. Zhang, *Energy Storage Mater.* **2021**, *41*, 248–254.
[19] L. Wang, W. Hua, X. Wan, Z. Feng, Z. Hu, H. Li, J. Niu, L. Wang, A. Wang, J. Liu, X. Lang, G. Wang, W. Li, Q.-H. Yang, W. Wang, *Adv. Mater.* **2022**, *34*, 2110279.
[20] Z. Li, L.-P. Hou, N. Yao, X.-Y. Li, Z.-X. Chen, X. Chen, X.-Q. Zhang, B.-Q. Li, Q. Zhang, *Angew. Chem. Int. Ed.* **2023**, *n/a*, e202309968.
[21] M. Kehrer, J. Duchoslav, A. Hinterreiter, M. Cobet, A. Mehic, T. Stehrer, D. Stifter, *Plasma Processes Polym.* **2019**, *16*, 1800160.
[22] P. Li, Z. Cheng, J. Liu, L. Che, Y. Zhou, E. Xu, X. Tian, Z. Yuan, *Small* **2023**, *n/a*, 2303149.
[23] Z. Liu, M. Chen, D. Zhou, Z. Xiao, *Adv. Funct. Mater.* **2023**, *n/a*, 2306321.
[24] Y. Xie, J. Cao, X. Wang, W. Li, L. Deng, S. Ma, H. Zhang, C. Guan, W. Huang, *Nano Lett.* **2021**, *21*, 8579–8586.
[25] Q. Zeng, X. Li, W. Gong, S. Guo, Y. Ouyang, D. Li, Y. Xiao, C. Tan, L. Xie, H. Lu, Q. Zhang, S. Huang, *Adv. Energy Mater.* **2022**, *12*, 2104074.
[26] L. Xue, Y. Li, A. Hu, M. Zhou, W. Chen, T. Lei, Y. Yan, J. Huang, C. Yang, X. Wang, Y. Hu, J. Xiong, *Small Structures* **2022**, *3*, 2100170.
[27] S. Lang, S.-H. Yu, X. Feng, M. R. Krumov, H. D. Abruña, *Nat. Commun.* **2022**, *13*, 4811.
[28] T. Lei, W. Chen, W. Lv, J. Huang, J. Zhu, J. Chu, C. Yan, C. Wu, Y. Yan, W. He, J. Xiong, Y. Li, C. Yan, J. B. Goodenough, X. Duan, *Joule* **2018**, *2*, 2091–2104.

Manuscript received: January 6, 2024
Accepted manuscript online: April 15, 2024
Version of record online: June 7, 2024

© 2024 The Authors. Angewandte Chemie International Edition published by Wiley-VCH GmbH

15213773, 2024, 28, Downloaded from https://onlinelibrary.wiley.com/doi/10.1002/anie.202400382 by Humboldt-Universitat Zu Berlin, Wiley Online Library on [06/01/2025]. See the Terms and Conditions (https://onlinelibrary.wiley.com/terms-and-conditions) on Wiley Online Library for rules of use; OA articles are governed by the applicable Creative Commons License